High Energy Density Physics 6 (2010) 381–390

Contents lists available at ScienceDirect

High Energy Density Physics

journal homepage: www.elsevier.com/locate/hedp

Laboratory astrophysics and non-ideal equations of state: the next challenges for astrophysical MHD simulations

Robert L. Carver [a,*], Andrew J. Cunningham [b,e], Adam Frank [b], Patrick Hartigan [a], Robert Coker [c], B.H. Wilde [c], John Foster [d], Paula Rosen [d]

[a] Rice University, Department of Physics and Astronomy, 6100 Main Street, Houston, TX 77521-1892, United States
[b] University of Rochester, Department of Physics and Astronomy, Rochester, NY 14627-0171, United States
[c] Los Alamos National Laboratory, Los Alamos, NM 87545, United States
[d] Atomic Weapons Establishment (AWE) Aldermaston, Reading Berkshire, RG7 4PR, United Kingdom
[e] Lawrence Livermore National Laboratory, Livermore, CA 94550, United States

ARTICLE INFO

Article history:
Received 26 August 2009
Received in revised form
22 January 2010
Accepted 22 January 2010
Available online 28 March 2010

Keywords:
Laboratory astrophysics
Astrophysical jets
Non-Ideal EOS
Hydrodynamics
Simulation
Omega Laser

ABSTRACT

Laboratory astrophysics holds great promise not only as a highly effective validation tool for astrophysical magneto-hydrodynamics (MHD) codes but it also presents a unique challenge for these codes. The high-density plasmas found in these experiments are not well modeled by the ideal equations of state (EOS) found in most astrophysical simulation codes. To solve this problem, we replaced the ideal EOS scheme in an existing MHD code, AstroBEAR, with a non-ideal EOS method and validated our implementation with van der Waals shock tube tests. The improved code is also able to model flows that contain more than one material, as required in laboratory experiments. Simulations of jet experiments performed at the OMEGA Laser reproduce the morphology of the jet much better than when the code used a single material and an ideal EOS.

1. Introduction

Hydrodynamical simulation codes are an essential tool in astrophysics research of phenomena as diverse as stellar outflows, supernovae, and accretion disks. These codes are separable into two main categories, Lagrangian and Eulerian. Lagrangian codes are characterized by a base grid of cells that are initialized with physical properties such as mass, temperature and velocity. These cells then move and change shape according to solutions to the Euler fluid dynamical equations. This approach essentially treats each cell as a particle that represents the average value for all the particles in that cell. Lagrangian codes can use grid cells of different shapes and sizes, allowing for large and geometrically complex initial grids. These codes work best when the flows are not overly complicated and are confined to a single dimension. For example, 1D star formation simulations of collapsing gas can be done very effectively with Lagrangian codes. However, as the flows become more complicated, cells may fold back onto themselves and the resulting tangled grid then requires a complicated regridding procedure. When multi-dimensional shocks occur, regridding inhibits the ability of a Lagrangian code to work effectively. Hence, most multi-dimensional codes designed to study stellar outflows and supernovae, where shocks play a key role in the hydrodynamics, are Eulerian.

Eulerian codes start with a similar base grid structure as Lagrangian codes except the control volumes remain static rather than moving with the flow. The fluxes of physical properties, such as mass density, are calculated for a system of conservation laws. In a conservative Eulerian code the flux out of a cell corresponds to a flux into another cell. Thus the physical variables in question, generally mass, energy, and momentum densities, are conserved over the whole simulation.

Hydrodynamical codes have evolved over the past decades to simulate more complicated flow structures, achieve higher resolutions, lessen computational times, and include additional physics. For example, expanding from 2D to 3D simulations was necessary to deal with more complicated flow structures, and adaptive mesh refinement codes (AMR; e.g FLASH [1], ENZO [2], and ORION [3])

* Corresponding author. Tel.: +1 713 775 7543; fax: +1 713 348 4150
E-mail address: bobby.carver88@gmail.com (R.L. Carver).

1574-1818/$ – see front matter © 2010 Elsevier B.V. All rights reserved.
doi:10.1016/j.hedp.2010.01.018

achieved faster computational times, resolved fine spatial scales in areas such as gravitational collapse, and captured shocks better than non-AMR codes. AMR is based on the concept of a cell size that adapts during the simulation, with changes in the cell size confined to the portions of the grid where smaller scale physics occurs. The ability to have more cells only where needed increases the computational efficiency of AMR codes, and parallelization also leads to increased ability to handle large scale problems.

Another major challenge for hydrodynamical codes has been to include magnetic fields, which play an important role in the hydrodynamics of many astrophysical phenomena, such as magnetized outflows and accretion disks. Such situations motivated the addition of magnetic fields to hydrodynamics codes to create magneto-hydrodynamics (MHD) codes. Codes such as ZEUS [4] were among the first to expand to MHD. Finally, many astrophysical situations require additional physics, e.g. molecule formation on dust grains [5], relativistic physics [6], and complex radiation transport [7]. MHD codes are constantly evolving to meet these challenges.

Laboratory astrophysics is the most recent challenge to face astrophysical MHD codes. This area of research uses high power lasers to generate flows and shocks [8], which have analogs to jets driven from young stars [9]. Magnetic pinch facilities, such as the Z-machine at Sandia National Laboratory, are also widely used in laboratory astrophysics research. Laboratory experiments provide a valuable validation tool not available to typical astrophysical codes. Astronomical observations only provide data on the part of a flow that radiates, but laboratory experiments generate more direct data about the hydrodynamics involved in the entirety of a particular flow. Therefore, a code validated via laboratory experiments allows for greater confidence in the validity of many other simulations done using that code. Unfortunately, the high-density plasmas associated with these laboratory experiments are not well approximated by the ideal gas equations of state (EOS) associated with most astrophysical MHD codes. Instead, some type of non-ideal gas equation of state capability must be added.

Incorporating a non-ideal equation of state into an astrophysical MHD code represents the next step if simulations are to keep pace with the technological advancements in laboratory astrophysics studies. This paper focuses on AstroBEAR [10], an Eulerian based code that has the 3D, MHD, AMR, and parallelization capabilities as described above. Given AstroBEAR's extensive use simulating the types of astrophysical flow structures that laboratory experiments are designed to reproduce, it provides a good base code upon which to build a non-ideal gas EOS capability for simulating these laboratory experiments.

In this paper, we will explore some differences between a non-ideal EOS and an ideal EOS framework. We will discuss the difficulties associated with incorporating a non-ideal EOS into an ideal EOS-based code and what changes were necessary to adapt AstroBEAR to a non-ideal gas code. We will also show the results from our first simulation of a laboratory experiment using AstroBEAR's non-ideal EOS capability. We will compare ideal EOS simulations, non-ideal EOS simulations, and experimental results. These comparisons demonstrate that codes using a non-ideal EOS framework can simulate laboratory environments more effectively than the ideal framework traditionally used in astrophysical codes.

2. Non-ideal EOS

Earlier versions of AstroBEAR had only ideal gas equation of state capability. For an ideal gas the energy density, ϵ, can be expressed by:

$$\epsilon = \frac{F}{2} n k_b T \tag{1}$$

with degrees of freedom F, temperature T, number density n, and Boltzmann's constant k_b. For an ideal gas, the adiabatic constant γ and the pressure P are given by:

$$\gamma = \frac{C_P}{C_V} + \frac{2+F}{F} \tag{2}$$

$$P = n k_b T = \frac{\rho k_b T}{\mu m_H} \tag{3}$$

where C_P and C_V are the specific heats of the gas at constant pressure and volume respectively, ρ is the mass density, m_H is the mass of hydrogen, and μ is the mean molecular weight. For example the mean molecular weight of titanium is defined by $\mu_{Ti} = m_{Ti}/(Z+1)$ with m_{Ti} equal to the molar mass of titanium and Z the ionization state of Ti, where $Z=0$ is neutral Ti. Combining Eqs. (1)–(3) yields the equation of state used by AstroBEAR when dealing with ideal gases:

$$P = (\gamma - 1)\epsilon \tag{4}$$

To utilize Eq. (3) to generate an ideal EOS for titanium we must know how μ depends on density and temperature. For a fixed density, as the temperature increases titanium becomes more ionized and μ decreases. For example, $\mu_{TiI} = 47.90$, $\mu_{TiII} = 23.95$, $\mu_{TiIII} = 15.97$, etc. To approximate μ as a function of temperature and density for the ideal case we use the Saha equation:

$$\frac{n_{i+1} n_e}{n_i} = 2\left(\frac{2\pi m_e k_b T}{h^2}\right)^{3/2} \frac{Z_{i+1}}{Z_i} e^{-X_i/(k_b T)} \tag{5}$$

where n_i and n_{i+1} represent adjacent ionization states, n_e is the electron number density, m_e is the electron mass, T is temperature, h is Planck's constant, χ_i is the ionization energy for the ith ionization state, and Z is the partition function. However at high temperatures the complicated level structure of a metal such as titanium makes the calculation of partition functions non-trivial. For the purposes of our ideal titanium EOS calculations we assumed the ratio of partition functions to be equal to 1. These partition function are of order unity and should not have a significant effect on the results generated using the Saha equation. For example, at a density of 1.0 g cm^{-3} and temperature of 10^5 K, using our partition function assumption yields a μ of 15.75 with TiII being the dominant ionization state. However if we set $Z_{TiIII}/Z_{TiII} = 2.0$, the Saha equation yields a μ of 14.95 only a 5% change from our previous result.

Fig. 1 compares the pressure–temperature dependence of this ideal EOS for titanium with a non-ideal EOS obtained from the SESAME [12] tables, discussed in more detail below. The dominant titanium species, from ideal calculations, is labeled on each figure. As expected, these plots show that as the gas moves into a lower density-higher temperature regime the ideal EOS and the SESAME EOS converge. However, as the gas moves towards higher density-lower temperature regimes the SESAME EOS begins to deviate from the ideal EOS with the non-ideal nature of the gas most evident as the density approaches the solid density of titanium, 4.5 g cm^{-3}.

The basic assumption that underlies the ideal gas equation is that there are only collisional interactions between particles. However high-density plasmas contain charged particles in relatively close proximity, leading to non-collisional interactions and to non-ideal gas behavior. There are three main effects that cause a non-ideal gas EOS to differ from the ideal EOS: Coulomb interaction, ionization potential perturbation, and electron degeneracy gas pressure.

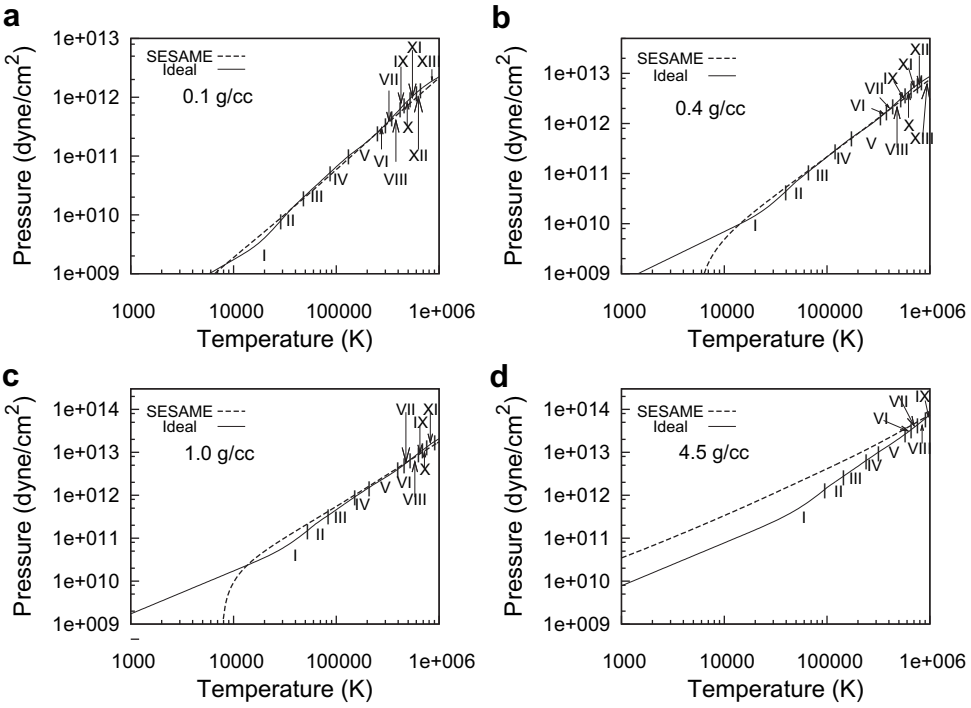

Fig. 1. Real vs. Ideal EOS for titanium. The Roman numerals denote the dominant ionization state of the Ti, as determined from the Saha equation.

At low number densities the Coulomb interaction between particles is an overall attractive effect. Positively charged ions attract negatively charged free electrons, known as Debye shielding. This attraction causes the ions to be more bound which in turn depresses the overall pressure of the gas. Debye shielding is significant so long as $n \ll 1.1 \times 10^5 (T/\overline{Z}^2)^3$ cm^{-3}, where T is in Kelvin and $\overline{Z}$ is the average ionization state of the gas [11]. For a gas with $\overline{Z} \sim 1$ at $T = 5.0 \times 10^4$ K, this condition is $n \ll 10^{19}$ cm^{-3}. In our experiments the number densities range from 10^{21} to 10^{22} cm^{-3}, so we can neglect the effects of Debye shielding in our calculations.

As the separation between ions decreases, Coulomb repulsion between the electrons bound to each ion increases. This interaction causes the electrons to become more loosely bound and results in an overall lower ionization potential at high densities. This ionization potential perturbation represents a major deviation from an ideal EOS for laboratory experiments and can be approximated by [11]:

$$\Delta \bar{I} = 2(\overline{Z}+1)e^3 \left[\frac{(\pi \overline{Z}(\overline{Z}+1)n)}{(k_b T)}\right]^{1/2} \quad (6)$$

where $\overline{Z}$ is the average ionization state of the ideal gas, n is the number density, and T is the temperature. For example, Ti gas with $\rho = 4.5$ g cm^{-3} and $T = 5.0 \times 10^4$ K has a change in average ionization potential of ~35 eV. Given that the sum of the first 3 ionization energies of Ti is ~45 eV we can expect that this will effectively raise the average ionization state of Ti from 1.0 to ~3.25. This increase in ionization will lead to a decrease in μ and thereby an increase in pressure by a factor ~3.25. As the temperature increases the ionization perturbation decreases leading to convergence of the ideal number density and the non-ideal number density at high temperatures. This non-ideal effect is seen in Fig. 1(d).

Finally, as the density of the gas increases, so does the importance of electron degeneracy pressure. Electron degeneracy is important when the temperature is on the order of or smaller than the electron degeneracy temperature $T_o = 4.5 \times 10^{-11} n^{2/3}$ K, where n(cm^{-3}) is the electron number density [11]. Again using titanium as an example, for $\rho = 0.1$ g cm^{-3}, $T_o = 5.0 \times 10^3$ K while for $\rho = 4.5$ g cm^{-3}, $T_o = 5.9 \times 10^4$ K. As a result, we can expect electron degeneracy pressure to have an effect for the high-density gases at temperatures ~10^5 K. The minimum electron degeneracy pressure, $P_d = (2.0 \times 10^{-11})\ k_b n^{5/3}$ dyne/cm^2 [11] where n is the electron number density (cm^{-3}) and k_b is Boltzmann's constant, for Ti gas at solid density and $T = 5.0 \times 10^4$ K is on the order of 2.0×10^{11} dyne/cm^2 for singly ionized Ti. This electron degeneracy pressure results in an increase in the pressure of a non-ideal gas relative to an ideal gas. As with the ionization potential, this effect will disappear at high temperatures well above the electron degeneracy temperature. The electron degeneracy pressure also vanishes at the lower temperatures when Ti is neutral. This non-ideal effect can be seen in Fig. 1(d).

The combination of Coulomb interactions, ionization potential perturbation and electron degeneracy will increase the pressure of a non-ideal gas relative to that of an ideal gas as the density of the gas increases. For example, at $T = 5.0 \times 10^4$ K, the factor of 3.25 increase in pressure associated with the ionization potential perturbation and the 2.0×10^{11} dyne/cm^2 increase in pressure associated with electron degeneracy explain the difference between the non-ideal and ideal gas pressures plotted in Fig. 1. Given that our experiments involve vaporized solids at high densities, the expected non-ideal nature of these gases makes using an ideal EOS insufficient to accurately simulate the hydrodynamics.

Another example of the need for non-ideal EOS is the simulation of a solid material. A solid by it's very nature implies that there are non-collisional interactions between particles. The strong bonding between particles restricts the ability of the particles to move freely. Therefore when energy is added to a solid this energy is used to break bonds before being used to increase kinetic energy, an obvious deviation from an ideal gas. Currently, AstroBEAR does not explicitly track the phase of a material; it instead relies on the

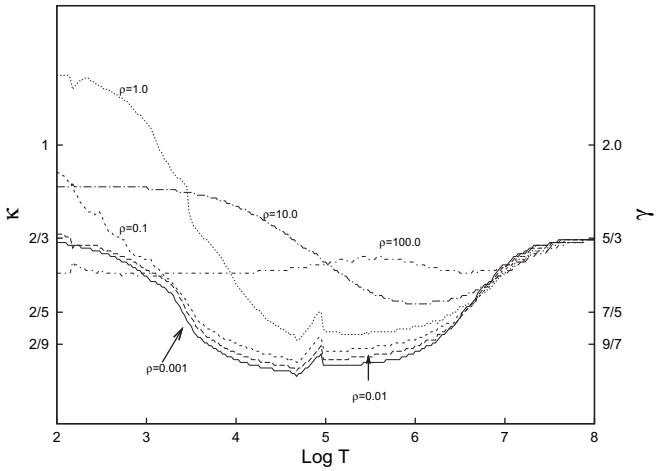

Fig. 2. Plot of κ as a function of temperature for Ti at different mass densities (g cm^{-3}).

SESAME tables which contain implicit phase behavior, mainly through the pressure derivatives. With solid materials, as with high-density plasmas, a non-ideal EOS must be used to model the laboratory experiments accurately.

We used the SESAME tables, provided by Los Alamos National Laboratory (LANL), to determine the non-ideal EOS for the materials of interest. The SESAME tables are a collection of tabular results for many different elements and materials from a variety of sources, and these tables provide an array of physical properties. Since our code uses pressure and pressure gradients to determine flow we used the SESAME tables for pressure as a function of mass density and temperature. Energy density is a conserved variable and not temperature, so the SESAME table for energy density as a function of temperature and mass density had to be inverted to allow for the calculation of temperature. The tabular entries are derived from a combination of experimentally observed values, theoretically determined values, and interpolated values. These tables also include a series of FORTRAN routines for retrieving values and for interpolation.

The derivative of pressure with respect to energy density at constant mass density is contained in the SESAME tables and plays an important role in the computational scheme described in Section 3. For an ideal gas, this derivative can be easily calculated from Eq. (4) as:

$$\kappa = \frac{\partial P}{\partial \epsilon}\Big|_{\rho} = \gamma - 1 \tag{7}$$

which is equal to 2/3 for both monatomic and non-relativistic electron degenerate gases. Therefore we expect that in the low density-low temperature and high temperature limits a gas will behave like an ideal gas and that κ will asymptotically approach 2/3. We also expect that at the highest densities when electron degeneracy is dominant κ will remain 2/3. In the non-ideal gas regime the energy is partitioned between increasing kinetic energy and ionization. In this sense ionization acts as an additional degree of freedom and decreases γ in much the same way that the rotational and vibrational modes of a molecule decrease γ. Therefore we expect κ to decrease in the ρ–T regions where ionization is important. Fig. 2, a plot of κ for titanium obtained from the SESAME tables, clearly shows these trends. The lowest and highest densities asymptote to $\sim$2/3 in low temperature limit and all densities asymptote to 2/3 in the high temperature limit. For the intermediate temperatures κ clearly drops as the gas begins to ionize and then returns to 2/3 when the gas becomes fully ionized. There is also a bump occurring at temperatures $\sim 8.0 \times 10^4$ K which corresponds to the transition from TiIV to TiV as the dominant ionization species. This increase is expected because TiV is an Ar-like closed shell and much more difficult to ionize. Hence, the partition of energy is shifted back towards increasing kinetic energy and thereby raising γ. The final feature to note in Fig. 2 is the rise of κ at low temperatures for densities where Ti is expected to be solid but not fully degenerate; these values of κ represent the phase information implicitly contained in the SESAME tables.

Another aspect of laboratory experiments that differs from many astrophysical situations is the need to simulate multiple materials (see Section 3). Previously AstroBEAR had no capability to handle multiple non-ideal materials. Since each material in a simulation will have a unique EOS, any modification to the code to include non-ideal EOS also necessarily requires multiple non-ideal material capability. The computational approach to multiple materials used here will be discussed in the following two sections.

3. Numerical methods

The Euler equations in Cartesian geometries are given by

$$\frac{\partial \mathbf{Q}}{\partial t} + \frac{\partial \mathbf{f}_x}{\partial x} + \frac{\partial \mathbf{f}_y}{\partial y} + \frac{\partial \mathbf{f}_z}{\partial z} = 0 \tag{8}$$

where $\mathbf{Q}$ and the flux matrix $\mathbf{f}_x$ are given by:

$$\mathbf{Q} = \begin{bmatrix} \rho & \rho v_x & \rho v_y & \rho v_z & E & \rho_T \end{bmatrix} \tag{9}$$

$$\mathbf{f}_x = \begin{bmatrix} \rho v_x & \rho v_x^2 + P & \rho v_y v_x & \rho v_z v_x & (E+P)v_x & \rho_T v_x \end{bmatrix} \tag{10}$$

$$\mathbf{f}_y = \begin{bmatrix} \rho v_y & \rho v_x v_y & \rho v_y^2 + P & \rho v_z v_y & (E+P)v_y & \rho_T v_y \end{bmatrix} \tag{11}$$

$$\mathbf{f}_z = \begin{bmatrix} \rho v_z & \rho v_x v_z & \rho v_y v_z & \rho v_z^2 + P & (E+P)v_z & \rho_T v_z \end{bmatrix} \tag{12}$$

where ρ is the mass density, E is the total energy density per unit volume, v_x is the fluid velocity along the x coordinate direction, v_y and v_z are the velocity components in the transverse direction, P is the gas pressure and ρ_T is a passive flow tracer. For the present study we have updated the implementation of the hydrodynamic Riemann solver of Roe [13] for an arbitrary equation of state. The Roe approach considers the Euler equations in an approximate linearized form,

$$\frac{\partial \mathbf{Q}}{\partial t} + \mathbf{A}_x \frac{\partial \mathbf{Q}}{\partial x} + \mathbf{A}_y \frac{\partial \mathbf{Q}}{\partial y} + \mathbf{A}_z \frac{\partial \mathbf{Q}}{\partial z} = 0 \tag{13}$$

The AstroBEAR code implements several integration schemes for advancing of conservation law systems as described in Section 2 of Cunningham et al. [10]. The code is implemented so that the system of conservation laws under consideration are specified by the eigenvalues, right eigenvectors and left eigenvectors of the system matrix $A_{x\,i,j} = \frac{\partial f_{x\,i}}{\partial Q_j}$. The linearized Euler equations are specified by the system matrix

$$\mathbf{A}_x(\mathbf{Q}) = \begin{bmatrix} 0 & 1 & 0 & 0 & 0 & 0 \\ \chi - v_x^2 + \kappa v^2/2 & -(\kappa-2)v_x & -\kappa v_y & -\kappa v_z & -\kappa & 0 \\ -v_x v_y & v_y & v_x & 0 & 0 & 0 \\ -v_x v_z & v_z & 0 & v_x & 0 & 0 \\ \chi - v_x H + \kappa v_x v^2/2 & -\kappa v_x^2 + H & -\kappa v_y v_x & -\kappa v_z v_x & \kappa v_x & 0 \\ \rho_T v_x/\rho & \rho_T/\rho & 0 & 0 & 0 & v_x \end{bmatrix} \tag{14}$$

where v = velocity, H = enthalpy per unit mass. Following the approach described by Mottura [14], we have defined the system matrix in terms of the pressure derivatives

$$H = \frac{P+E}{\rho} \tag{15}$$

$$\chi = \frac{\partial P}{\partial \rho}\Big|_{\epsilon} \tag{16}$$

$$\kappa = \frac{\partial P}{\partial \epsilon}\Big|_{\rho} \tag{17}$$

to implement arbitrary equation of state capability where $=E-\rho v^2/2$ is the thermal energy per unit volume. In terms of the pressure derivatives, the sound speed is defined as

$$c = \sqrt{\chi + \kappa\left(H - \frac{1}{2}v^2\right)} \tag{18}$$

The desired eigenvalues are given as the components of the vector

$$\boldsymbol{\lambda} = [\,v_x - c \quad v_x \quad v_x \quad v_x \quad v_x \quad v_x + c\,]^{\mathrm{T}} \tag{19}$$

the corresponding right eigenvectors are the columns of the matrix

$$\mathbf{R} = \begin{bmatrix} 1 & 0 & 0 & 1 & 0 & 1 \\ v_x - c & 0 & 0 & v_x & 0 & v_x + c \\ v_y & 1 & 0 & v_y & 0 & v_y \\ v_z & 0 & 1 & v_z & 0 & v_z \\ H - v_x c & v_y & v_z & v^2/2 & 0 & H + v_x c \\ \rho_T/\rho & 0 & 0 & 0 & 1 & \rho_T/\rho \end{bmatrix} \tag{20}$$

and the corresponding left eigenvectors are the rows of the matrix

$$\mathbf{L} = \begin{bmatrix} \frac{c^2 + c v_x + \kappa\left(u^2 - H\right)}{2c^2} & \frac{-\kappa v_x - c}{2c^2} & \frac{-\kappa v_y}{2c^2} & \frac{-\kappa v_z}{2c^2} & \frac{\kappa}{2c^2} & 0 \\ -v_y & 0 & 1 & 0 & 0 & 0 \\ -v_z & 0 & 0 & 1 & 0 & 0 \\ \frac{\kappa\left(H - v^2\right)}{c^2} & \frac{\kappa v_x}{c^2} & \frac{\kappa v_y}{c^2} & \frac{\kappa v_z}{c^2} & \frac{-\kappa}{c^2} & 0 \\ \frac{\rho_T\left(1 + \kappa\left(H - v^2\right)\right)}{c^2} & \frac{\rho_T \kappa v_x}{c^2} & \frac{\rho_T \kappa v_y}{c^2} & \frac{\rho_T \kappa v_z}{c^2} & \frac{-\rho_T \kappa}{c^2} & 1 \\ \frac{c^2 - c v_x + \kappa\left(u^2 - H\right)}{2c^2} & \frac{-\kappa v_x + c}{2c^2} & \frac{-\kappa v_y}{2c^2} & \frac{-\kappa v_z}{2c^2} & \frac{\kappa}{2c^2} & 0 \end{bmatrix} \tag{21}$$

The Marquina [16] flux function implemented in the code calls for the computation of the above eigen decomposition of fluid states that are interpolated to the left, Q_L and right edge, Q_R, of each computational cell interface. The Roe [10] flux option in the code, on the other hand, calls for the decomposition of a suitably averaged interfaces state. The density, fluid velocity and enthalpy are given by

$$\rho = \sqrt{\rho_L}\sqrt{\rho_R} \tag{22}$$

$$\mathbf{v} = \frac{\mathbf{v}_L\sqrt{\rho_L} + \mathbf{v}_R\sqrt{\rho_R}}{\sqrt{\rho_L} + \sqrt{\rho_R}} \tag{23}$$

$$H = \frac{H_L\sqrt{\rho_L} + H_R\sqrt{\rho_R}}{\sqrt{\rho_L} + \sqrt{\rho_R}} \tag{24}$$

$$\rho_T = \frac{\rho_{T\,L}\sqrt{\rho_L} + \rho_{T\,R}\sqrt{\rho_R}}{\sqrt{\rho_L} + \sqrt{\rho_R}} \tag{25}$$

and for a general equation of state, an interface average of the pressure derivatives is also required. For the present work we have used the arithmetic average

$$\kappa = \frac{\kappa_L + \kappa_R}{2} \tag{26}$$

$$\chi = \frac{\chi_L + \chi_R}{2}. \tag{27}$$

Because the code utilizes the arithmetic averaged linearized Riemann solver of Ryu and Jones [17] for magnetohydrodynamical problems, we expect this choice of pressure derivative averaging will allow simpler extension for MHD problems.

4. Validation testing

We used the van der Waals EOS and the series of four shock tube problems named WV1, DG1, DG2, and DG3 by Guardone and Vigevano [18] to validate the implementation of the method described in Section 3. With this van der Waals EOS, pressure and its derivatives are given by:

$$P = \delta\frac{E + a\rho^2}{1 - b\rho} - a\rho^2 \tag{28}$$

$$\chi = \delta\frac{b\left(E - a\rho^2\right) + 2a\rho}{\left(1 - b\rho\right)^2} - 2a\rho \tag{29}$$

$$\kappa = \frac{\delta}{1 - b\rho} \tag{30}$$

where a and b are the van der Waals constants, E is thermal energy density, ρ is mass density, $\delta = (R)/(\mu_o c_v)$, μ_o is the mean molecular weight, c_v is the specific heat at constant volume, and R is the universal gas constant.

Figs. 3 and 4 show the shock tube test problem results and Table 1 shows the initial conditions for the four tests, where pressure and density are defined relative to the critical values $P_{\mathrm{crit}} = a/(27b^2)$ and $\rho_{\mathrm{crit}} = 1/(3b)$. These 1D simulations contained 400 cells from $x = 0$ to 1.0 with the density and pressure jumps initially occurring at $x = 0.5$. In each plot, the results obtained from AstroBEAR's ideal EOS are plotted against the results from AstroBEAR's van der Waals EOS. In all four cases AstroBEAR's non-ideal Roe implementation scheme shows excellent agreement with the results found in Guardone and Vigevano [18].

5. Problem setup

The code utilizes advective tracers to track how different materials move. The advection equation

$$\frac{\partial \rho_T}{\partial t} + \frac{\partial \rho_T v_x}{\partial x} + \frac{\partial \rho_T v_y}{\partial y} + \frac{\partial \rho_T v_z}{\partial z} = 0 \tag{31}$$

sets up an advected density for each different material. Initially all cells are defined to be a single material, and each different material involved in the simulation is assigned its own tracer. At any point in the simulation a combination of the conserved variable of mass density and the value of each material's tracer define the mass percentage of each material in that cell. These percentages combined with the total mass density flux of a particular cell determine the flux for each material in that cell. For example, a pure titanium cell at a density of 4.5 g cm^{-3} has a titanium tracer value of 4.5, while other tracers are assigned value of 0.0. The fractional energy density of each material is also necessary. The fraction of each cell's energy that is assigned to a particular material is determined by using a weighted average. The mass fraction of a material combined with its molar mass is used to calculate the molar fraction of that material for that cell. The energy density fraction is defined to be the same as the mole fraction of a material in a cell. After determining the mass fraction and energy fraction for

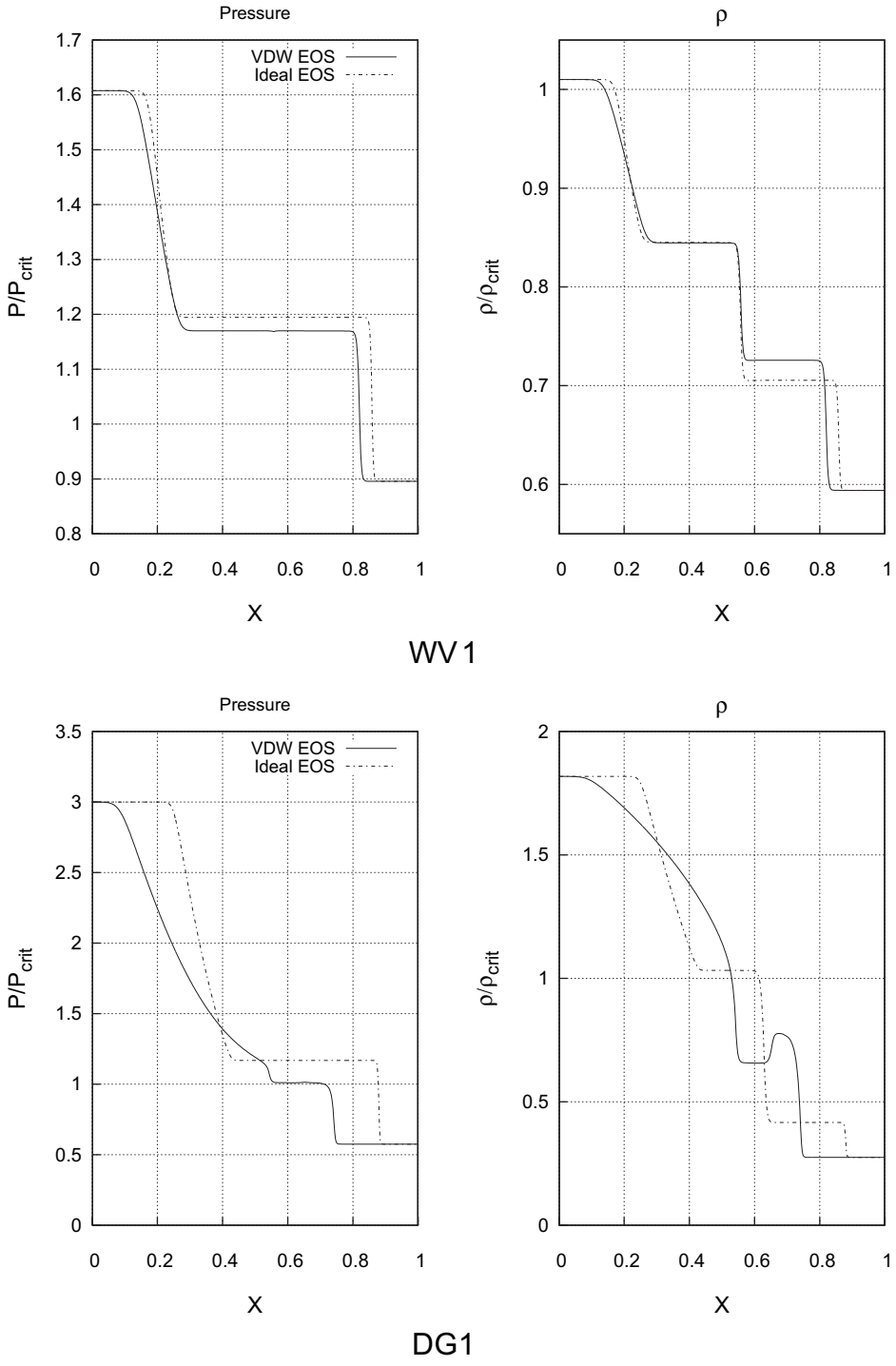

Fig. 3. van der Waals tests WV1 at $t = 0.2$ and DG1 at $t = 0.15$.

a material in a particular cell, these values are used to look up the values for pressure, χ, and κ from the SESAME tables. The final χ and κ for an entire cell are the weighted averages of the χ's and κ's of each material in the cell, based on their molar fraction of the material. The mixed material cells are assumed to be fully mixed gases. The total pressure for the cell is defined to the sum of the SESAME pressure for each material.

These material tracers will undergo the same numerical diffusion as any other fluid quantity advected through the grid due to the second order accuracy of the time advance algorithm. We track the individual fluid species in a manner that is both conservative and consistent with the advection of the total fluid density using the method of Plewa and Muller [19]. This method renormalizes the fluid tracer fluxes computed by the integration scheme to be equal to the flux of the total fluid density at each grid cell interface. However, AstroBEAR does not have explicit interface tracking and thus material interfaces still will get spread over a few zones in a manner that is determined by numerical diffusion.

Fig. 5 shows the schematic of the target used in designing the simulation's initial conditions [20], with all material boundaries

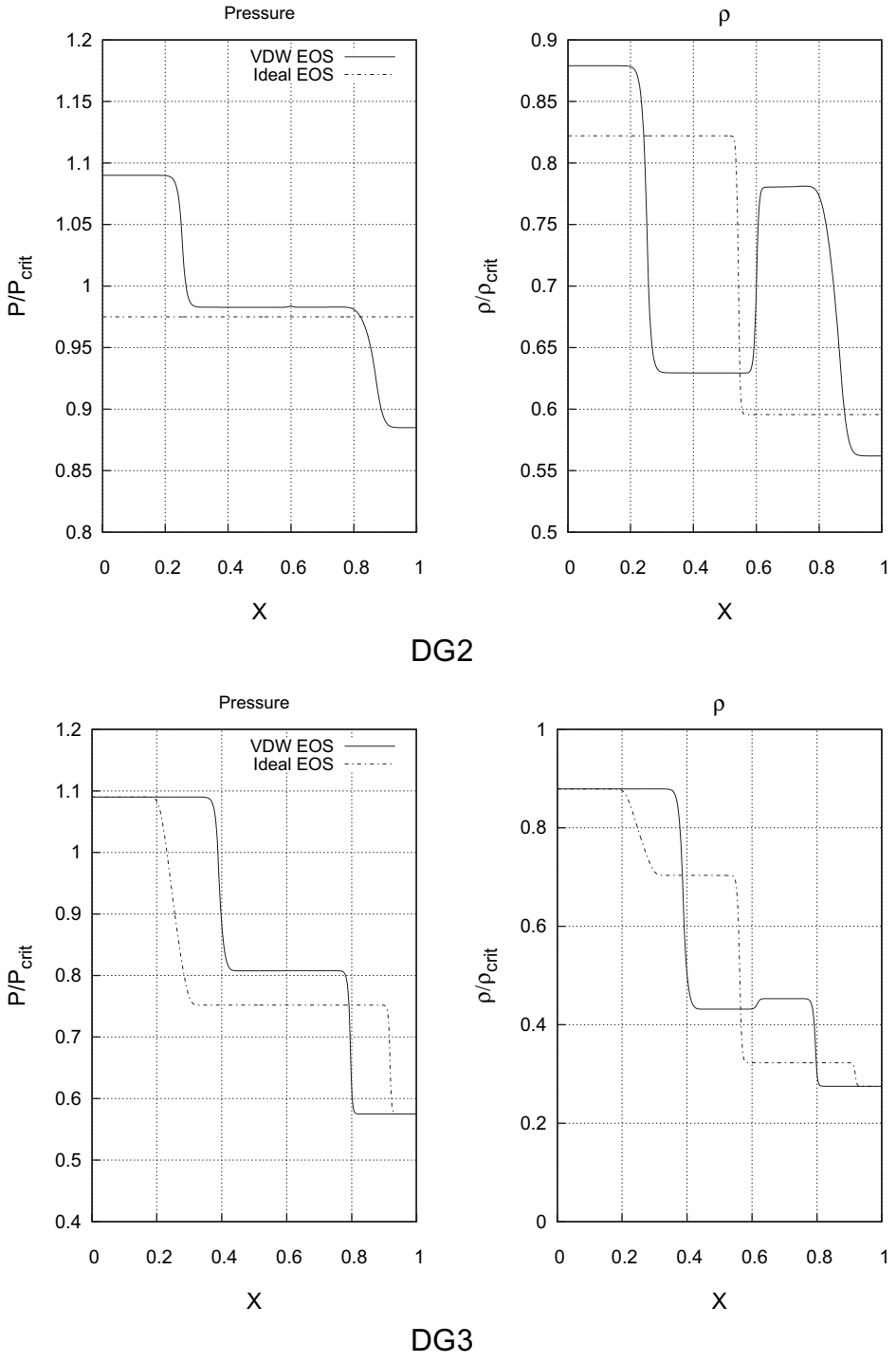

Fig. 4. van der Waals tests DG2 at $t = 0.45$ and DG3 at $t = 0.2$.

initially mesh aligned. The titanium plate and washer are defined to be initially at 300 K at a density of 4.4467 g cm^{-3} using SESAME table 2961. The foam is defined using the CH SESAME table 7592 at a temperature of 300 K and a density of 0.1 g cm^{-3}. The vacuum space inside the washer was defined using the dry air SESAME table 5030 at a temperature of 300 K and a density of 0.001 g cm^{-3}. Simulations are 3.0 mm by 2.0 mm with a resolution of 8 μm, using a 360×240 mesh. Extrapolating boundaries were used for the left, right and top boundaries and a reflecting boundary was used for the bottom. The second order accurate MUSCL-Hancock integration method was used. The linearized Roe solver was used for solving the flux function as described earlier. Simulations were run for approximately 150 ns. Laser deposition occurs in the hohlraum on the left edge of Fig. 5 heating it up to temperatures on the order of 10^6 K. The peak blackbody radiation at these temperatures is X-ray, which illuminates the left side of the titanium plate not covered by the gold washer. It drives ablated material to the left and a strong shock to the right.

The simulation of laboratory experiments also should include a treatment of the laser used to drive the experiment. As an

Table 1
van der Waals shock tube initial conditions

Test	P_l	ρ_l	P_r	ρ_r
WV1	1.60770	1.010	0.8957	0.594
DG1	3.00	1.818	0.5750	0.275
DG2	1.09	0.879	0.8850	0.562
DG3	1.09	0.879	0.5750	0.275

astrophysical based code, AstroBEAR was not designed with any type of laser deposition capability. The code does not currently have the physics necessary to simulate laser deposition. Therefore, we approximated the pressure drive from the laser using the hydro code RAGE [15] out of LANL, which does have ablation simulation capability. RAGE was able to generate a pressure profile as a function of time along the laser deposition surface. This pressure profile allowed us to calculate energy densities necessary to generate the proper pressure in the deposition layer of the titanium surface. Currently the deposition layer is defined to be the ghost zones to the left of the simulated target and vertically up to the beginning of the gold layer as shown in Fig. 5. These cells are specifically defined as a function of time to have the necessary energy density needed to recreate the pressure profile provided by LANL. Fig. 6 is a plot of the pressure profile used in the simulation. The *x*-axis shows time in ns after the beginning of the laser pulse. The *y*-axis shows the pressure inside the deposition layer in dyne/cm^2. This approximation of the laser pulse will not simulate all of the physics involved in the laser drive and will cause the simulated results to differ from experimental results.

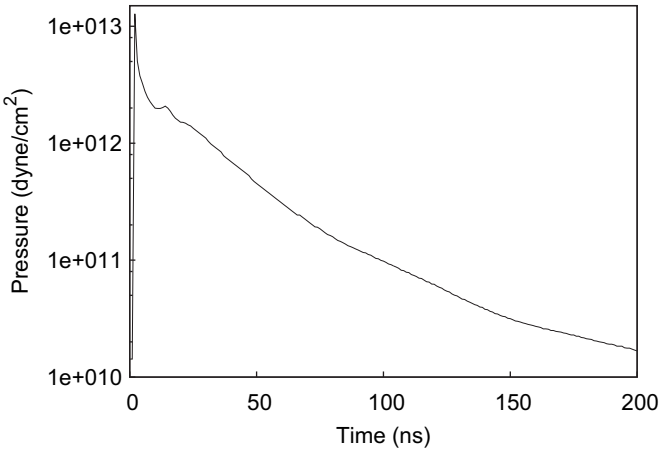

Fig. 6. LANL pressure profile used to simulate laser drive.

6. Results and analysis

Fig. 7 shows a comparison of 2D cylindrically symmetric AstroBEAR simulations and experimental data at 100 ns after the laser drive. Panel (a) depicts a simulated radiograph from an ideal EOS setup containing only neutral hydrogen, using the drive pressure profile provided by LANL. Panel (b) is a simulated radiograph from a simulation using the same setup, but with the newly implemented SESAME based non-ideal EOS with multiple materials instead of the single material ideal EOS. Panel (c) is actual experimental data. Features of note in the experimental data include the shock front position, shock width, and the presence of an interior flute-like jet. This interior jet is caused by the collapse and subsequent rebounding of the walls of the titanium washer after vaporized titanium has accelerated through the vacuum [20] The simulated radiographs have been grey-scaled to give an accurate representation of the structure of the jet but have not been matched in grey-scaling to the experimental radiograph.

Fig. 8 plots the position of the jet head as a function of time in the experiment and the simulations, where distance is measured from the face of the titanium washer. Both the ideal and non-ideal simulations are in reasonably good agreement with the experimental data, although the position of the head is approximately 35% ahead of the experimental data. This discrepancy is most likely caused by the approximation of the laser pulse using the pressure profile in Fig. 6. Small changes to the pressure profile affect the position of the head with respect to time without significantly affecting the morphology of the jet.

The ideal EOS radiograph shows obvious inaccuracies in simulating the laboratory environment. While the position of the shock front is similar to the experimental data, the ideal radiograph bears almost no morphological resemblance to the experiment. In contrast, the non-ideal EOS simulation shows dramatic improvement in modeling the overall morphology of the experiment. The non-ideal simulation reproduces both the lateral shock and a flute-like shape for the interior jet, key factors missing from the ideal simulation. Remaining differences between the non-ideal simulation of the interior jet and that seen in the experiment arise in part because of the ideal treatment of cells with mixed materials

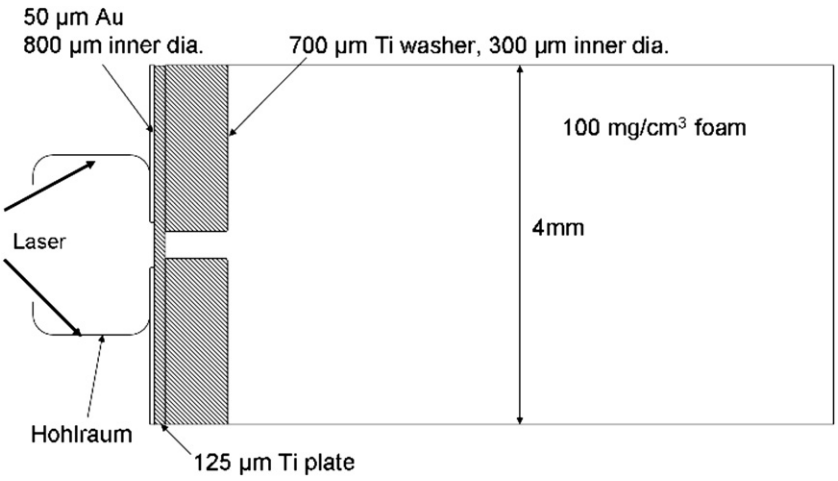

Fig. 5. Laser target schematic.

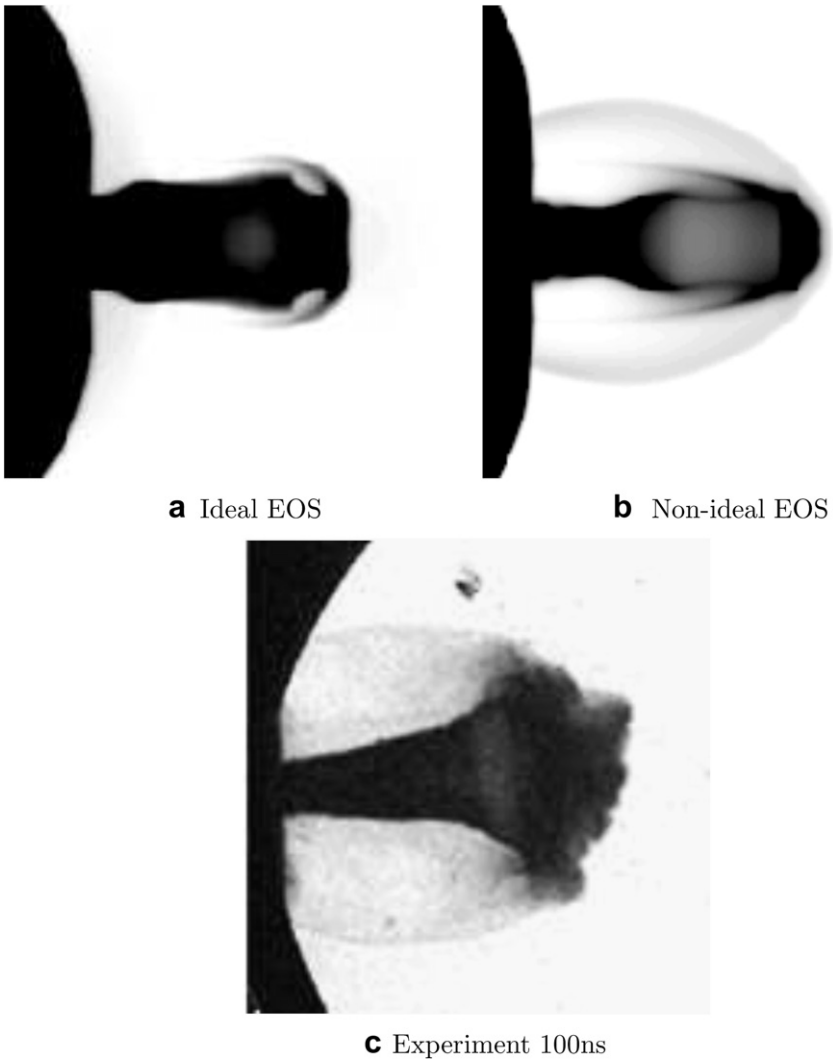

Fig. 7. Simulation comparison.

(Section 3). These mixed cells occur as the jet forms from the collapse of the washer, and are important for determining how the jet evolves.

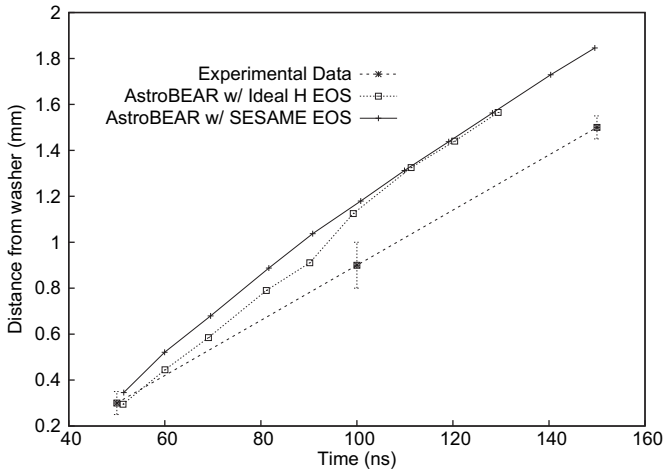

Fig. 8. Jet head position vs. time comparison for AstroBEAR with SESAME EOS, AstroBEAR with ideal H EOS, and experimental results.

7. Summary

A non-ideal EOS and a capability to handle multiple non-ideal materials was successfully added to the astrophysical MHD code, AstroBEAR. Redefining the flux function in terms of pressure and its derivatives proved to be more successful than forcing a non-ideal EOS into an ideal EOS framework. Our first non-ideal EOS simulations from AstroBEAR show that a non-ideal EOS framework is clearly preferable to an ideal EOS for the simulation of laboratory experiments.

While the basic capability for using non-ideal EOS has been achieved, plenty of room exists for further improvement. For example, including the physics necessary to properly simulate the laser drive will lead to better models of the jet's evolution. The calculation of mixed cells involving solids and gases may be improved, and a more sophisticated treatment of energy splitting for mixed cells can be implemented, taking into account a mixed cell with different states of matter. Finally, the 8 μm resolution of these simulation is insufficient to capture all of the morphological detail present in the experimental data. Further simulations will require 3D simulations at higher resolution to more accurately predict experimental results. AstroBEAR now has stable basic implementation of a non-ideal EOS capability upon which these improvements can be added.

Acknowledgements

This research was made possible through DOE/NNSA grants DE-PS52-08NA28649 and DE-FG52-07NA28056 to PMH under the NLUF program. This work was supported in part by the Shared University Grid at Rice funded by NSF under Grant EIA-0216467, and a partnership between Rice University, Sun Microsystems, and Sigma Solutions, Inc.

Support for A.F. was in part provided by NASA through awards issued by JPL/Caltech through Spitzer program 20269, the National Science Foundation through grants AST-0406823, AST-0507519 and PHY-0552695 as well as the Space Telescope Science Institute through grants HST-AR-10972, HST-AR-11250, HST-AR-11252. We also thank the University of Rochester Laboratory for Laser Energetics and funds received through the DOE Cooperative Agreement No. DE-FC03-02NA00057.

A.J.C.'s contribution to this work was performed under the auspices of the U.S. Department of Energy by Lawrence Livermore National Laboratory under Contract DEAC5207NA27344. LLNL-JRNL-415701 B.H.W.'s and R.C.C.'s contributions to this work were supported by the US Department of Energy under Contracts No. W-7405-ENG-36 (LANL). J.F.'s and P.R.'s contributions to this work were performed under the direction of AWE.

References

[1] B. Fryxell, K. Olson, P. Ricker, F.X. Timmes, M. Zingale, D.Q. Lamb, P. MacNeice, R. Rosner, J.W. Truran, H. Tufo, FLASH: an adaptive mesh hydrodynamics code for modeling astrophysical thermonuclear flashes. Astrophysical Journal Supplement Series 131 (2000) 273–334.

[2] B.W. O'Shea, G. Bryan, J. Bordner, M.L. Norman, T. Abel, R. Harkness, A. Kritsuk, Introducing Enzo, an AMR cosmology application. ArXiv Astrophysics e-prints (2004).

[3] M. Herman, R. Capote, B.V. Carlson, P. Obložinský, M. Sin, A. Trkov, H. Wienke, V. Zerkin, EMPIRE: nuclear reaction model code system for data evaluation. Nuclear Data Sheets 108 (2007) 2655–2715.

[4] J.M. Stone, M.L. Norman, ZEUS-2D: a radiation magnetohydrodynamics code for astrophysical flows in two space dimensions. Astrophysical Journal Supplement Series 80 (1992) 753–790.

[5] A. Zsom, C.P. Dullemond, A representative particle approach to coagulation and fragmentation of dust aggregates and fluid droplets. Astronomy and Astrophysics 489 (2008) 931–941.

[6] J.C. McKinney, General relativistic magnetohydrodynamic simulations of the jet formation and large-scale propagation from black hole accretion systems. Monthly Notices of the Royal Astronomical Society 368 (2006) 1561–1582.

[7] R. Buras, M. Rampp, H.T. Janka, K. Kifonidis, Two-dimensional hydrodynamic core-collapse supernova simulations with spectral neutrino transport. Astronomy and Astrophysics 447 (2006) 1049–1092.

[8] Foster, J.M. and Wilde, B.H. Rosen, P.A. and Williams, R.J.R Blue, B.E Coker, R.F. Drake, R.P Frank, A Keiter, P.A Khokhlov, A.M Knauer, J.P Perry, T.S. High-energy-density laboratory astrophysics studies of jets and bow shocks. Astrophysical Journal Letters, 634:L77–L80

[9] B. Reipurth, J. Bally, Herbig-Haro flows: probes of early stellar evolution. Annual Review of Astronomy and Astrophysics 39 (2001) 403–455.

[10] A.J. Cunningham, A. Frank, P. Varniere, S. Mitran, T.W. Jones, Simulating magnetohydrodynamical flow with constrained transport and adaptive mesh refinement; algorithms and tests of the AstroBEAR code. Astrophysical Journal Supplement 182 (2009) 519–542.

[11] Y.B. Zel'Dovich, Y.P. Raizer, Physics of shock waves and high-temperature hydrodynamic phenomena. Academic Press, New York, NY, 1967, pp. 215–232.

[12]. P. Lyon, J.D. Johnson, SESAME: the Los Alamos National Laboratory Equation of State Database, LANL Technical Report LA-UR-92-3407. Los Alamos National Laboratory, Los Alamos, NM, 1992.<http://t1web.lanl.gov/newweb_dir/t1sesame.html>.

[13] P.L. Roe, Approximate Riemann solvers, parameter vectors, and difference schemes. Journal of Computational Physics 43 (1981) 357.

[14] L. Mottura, An evaluation of Roe's scheme generalizations for equilibrium real gas flows. Journal of Computational Physics 138 (Dec. 1997) 354–399.

[15] Michael Gittings, Robert Weaver, Michael Clover, Thomas Betlach, Nelson Byrne, Robert Coker, Edward Dendy, Robert Hueckstaedt, Kim New, WRob Oakes, Dale Ranta, Ryan Stefan, The RAGE radiation-hydrodynamic code. Computational Science and Discovery 1 (2008) 15005.

[16] R. Donat, A. Marquina, Capturing shock reflections: an improved flux formula. Journal of Computational Physics 125 (1996) 42–58.

[17] D. Ryu, T.W. Jones, Numerical magnetohydrodynamics in astrophysics: algorithm and tests for one-dimensional flow. Astrophysical Journal 442 (1995) 228–258.

[18] A. Guardone, L. Vigevano, Roe linearization for the van der Waals gas. Journal of Computational Physics 175 (2002) 50–78.

[19] T. Plewa, E. Müller, The consistent multi-fluid advection method. Astronomy and Astrophysics 342 (1999) 179–191.

[20] P. Hartigan, J.M. Foster, B.H. Wilde, R.F. Coker, P.A. Rosen, J.F. Hansen, B.E. Blue, R.J.R. Williams, R. Carver, A. Frank, Laboratory experiments, numerical simulations, and astronomical observations of deflected supersonic jets: application to HH110. The Astrophysical Journal 705 (2009) 1073–1094.